Terahertz Emission from Bismuth Thin Films Induced by Excitation with Circularly Polarized Light

Yoshua Hirai[1,*] Naotaka Yoshikawa,[1] Hana Hirose,[1] Masashi Kawaguchi,[1]
Masamitsu Hayashi,[1] and Ryo Shimano[1,2]

[1]*Department of Physics, The University of Tokyo, 7-3-1 Hongo, Bunkyo-ku, Tokyo, 113-0033, Japan*
[2]*Cryogenic Research Center, The University of Tokyo, 2-11-16 Yayoi, Bunkyo-ku, Tokyo, 113-0032, Japan*

We demonstrate that Bi thin films emit terahertz radiation when irradiated by circularly polarized femtosecond laser pulses. Terahertz emission that is polarized in a direction perpendicular to the plane of incidence is significantly enhanced when the pump pulse is circularly polarized compared with when it is linearly polarized. The enhanced terahertz emission reverses its polarity with the reversal of pump helicity. This helicity dependent terahertz emission is absent in the horizontal direction along the plane of incidence, and is odd with respect to the incident angle. Combined with the layer thickness dependence measurement, the dominant origin of terahertz emission is attributed to the photoinduced inverse spin Hall effect (ISHE) in Bi. The temporal dynamics of the ultrafast photocurrents are extracted and the spin and charge dynamics are discussed. The observation of terahertz emission from the photoinduced ISHE in a thin film consisting of a single material indicates the unique character of Bi, i.e., the long spin diffusion length and the large spin Hall angle, demonstrating the potential ability of the material to be applied to terahertz emitters and terahertz spintronics.

I. INTRODUCTION

Terahertz technology has greatly developed over the last few decades, promoting multiple areas of applications including sensing, imaging, spectroscopy, and high-speed communication. One typical method to obtain terahertz waves is the coherent terahertz pulse emission from ultrafast photocurrents or polarization currents induced by femtosecond laser pulse excitation. The induced photocurrents evolve following the envelope of the femtosecond pulses in a subpicosecond timescale, causing radiation of electromagnetic waves via dipole radiation in the terahertz regime. The photocurrent-induced terahertz radiation is given by $E_{\mathrm{THz}}(t) \propto \partial J(t)/\partial t$, where $E_{\mathrm{THz}}(t)$ is the electric field of the terahertz wave and $J(t)$ is the transient current. Terahertz emission by transient photocurrents has been intensively studied on a variety of quantum materials such as graphene [1,2], topological insulators [3,4], Weyl semimetals [5–7], and Rashba systems [8]. In particular, photocurrents generated by circularly polarized light [referred to as circular photocurrents (CPCs) hereafter] have been investigated by terahertz emission measurements and transport measurements [9–13]. CPCs are in some cases spin-polarized [4,7–9,13], and the generation of such CPCs by femtosecond laser pulses opens

a route to the ultrafast manipulation and generation of spin currents. Such features are thought to be essential for the development of ultrafast spintronic devices. Away from CPCs, ultrafast spin currents in magnetized ferromagnetic metal/nonmagnetic metal heterostructures have been demonstrated to induce efficient terahertz emission [14]. Here, the spin current is injected from the ferromagnetic metal layer, which is magnetized by an external magnetic field, and the spin current is converted into a transverse charge current due to the inverse spin Hall effect (ISHE) of the nonmagnetic metal layer. Compared with the scheme of spin current injection adopted in ferromagnetic metal/nonmagnetic metal heterostructures, terahertz emitters based on ultrafast CPCs have unique benefits as they do not require external fields, and the pump-helicity dependence of CPCs enables all-optical control (i.e., control without external fields) of the terahertz phase [5,8] and even the terahertz helicity [2,6].

CPCs are usually decomposed into two different contributions: the circular photogalvanic effect (CPGE) and the circular photon drag effect (CPDE) [2,10]. The two are distinguished by symmetry conditions: the former is forbidden for systems possessing inversion symmetry while the latter is not. In addition, there is another effect, namely the photoinduced ISHE [15]. The contribution from the ISHE in CPCs is usually very small because of the short spin relaxation time [9]. Therefore, experimental verification

*hirai@thz.phys.s.u-tokyo.ac.jp

has been limited to special cases such as GaAs/Pt heterostructures [15], where the combination of materials with a long spin relaxation time (GaAs) and a large spin Hall angle (Pt) makes the effect observable.

Bi is expected to host such spin and pump-helicity dependent photocurrents due to its large spin Hall angle and long spin diffusion length [16]. Moreover, it has been theoretically demonstrated that the giant spin Hall conductivity arises from the large Berry curvature associated with the Dirac point at the L point [17,18]. CPCs have also been recently observed in Bi thin films and Bi-based heterostructures by transport measurements [19]. Bi is well known to be the basis of many topological insulators, and thus the understanding of CPCs in Bi may shed light on the basic understanding of CPCs in Bi-based topological insulators.

In this paper, we investigate how CPCs in Bi thin films can be extended to the terahertz frequency range. Under the irradiation of a near-infrared (NIR) femtosecond laser pulse, we indeed observe terahertz emission from Bi thin films. From systematic measurements of pump-helicity dependence, polarization properties of the emitted terahertz wave and the Bi layer thickness dependence, we elucidate that the dominant origin of the terahertz emission is attributed to the photoinduced ISHE.

II. EXPERIMENTAL SETUP

The film samples are deposited via radio frequency magnetron sputtering on quartz substrates. A schematic of the sample structure is shown in Fig. 1(a). The thickness of the Bi layer is varied as $d = 30$, 50, 70, and 100 nm. The Ta and MgO layers act as cap layers to prevent oxidation and degradation of the Bi layer. We find from X-ray diffraction measurements that Bi is polycrystalline with grains predominantly oriented along the (111) and (110) directions (based on rhombohedral representation) [20,21].

A femtosecond pulse laser (central wavelength, 800 nm; pulse duration, 100 fs; repetition rate, 1 kHz; fluence, 120 $\mu J/cm^2$) is used for excitation. The excitation pulse is irradiated on the sample in oblique incidence with the incident angle $\theta \sim 45°$. A polarizer and a quarter wave plate (QWP) are placed in front of the sample. The pump helicity is controlled by changing the rotation angle α of the QWP. All measurements are made at room temperature under ambient pressure.

The emitted terahertz waves are collected by an off-axis parabolic mirror and focused onto a 1-mm-thick (110)-ZnTe crystal, where the conventional electro-optic (EO) sampling method is used to measure the terahertz waves in the time domain. Between the sample and the ZnTe crystal, a wire grid polarizer (WGP) is placed to restrict the polarization of the propagating terahertz wave to one of two choices: polarized horizontally (referred to as "X polarization" hereafter) or perpendicular [referred to as "Y
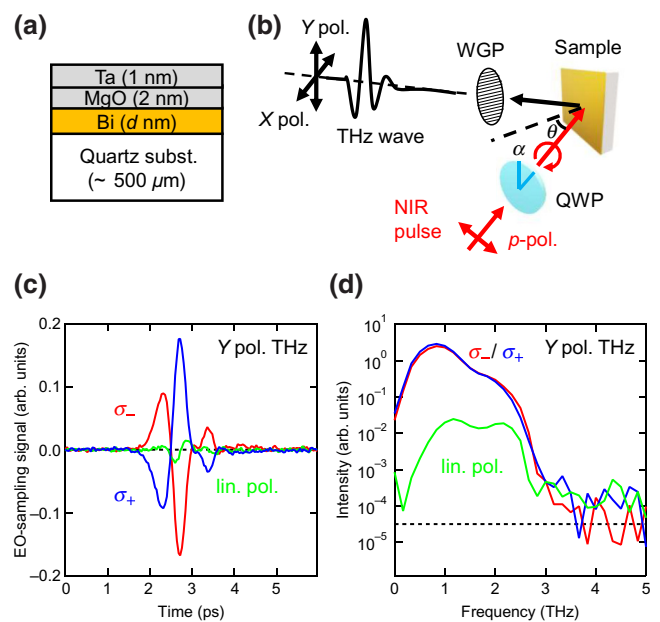

FIG. 1. (a) Schematic of the sample structure. (b) Schematic of the experimental setup. The incident angle is set to be $\theta \sim 45°$. The polarization of the excitation pulse can be changed from right circular polarization σ_+ to left circular polarization σ_-, or an elliptical polarization in between. WGP is wire grid polarizer, QWP is quarter wave plate. (c) Waveform of the emitted terahertz pulse from 30-nm-thick sample. Red and blue curves are obtained when the excitation pulse is circularly polarized. The green curve is obtained when the excitation pulse is linearly (p-) polarized. (d) The corresponding power spectra of the emitted terahertz wave.

polarization" hereafter, see Fig. 1(b)] to the plane of incidence. We mainly focus on the Y polarization, since it is the direction in which CPCs are expected to flow.

III. RESULTS

Typical waveforms of the measured terahertz waves are displayed in Fig. 1(c) along with their power spectra in Fig. 1(d). The polarity of the terahertz wave shows clear reversal when the pump helicity is reversed, and in either helicity the terahertz emission is enhanced significantly compared with linearly polarized excitation. Note that the high-frequency cutoff of the power spectrum around 2.5 THz is due to the use of ZnTe as the EO sampling crystal.

In order to study the detailed helicity dependence of the emitted terahertz wave, we use the EO sampling signal at the peak position as a measure of amplitude of the terahertz wave, and investigate the helicity dependence of the peak height. Typical helicity dependence of the peak height is shown in Fig. 2(a). Obtained helicity dependence for all Bi layer thicknesses are well fitted by a phenomenological

equation [9]

$$S_{\text{THz,peak}}(\alpha) = C \sin 2\alpha + L_1 \sin 4\alpha + L_2 \cos 4\alpha + D \quad (1)$$

where $S_{\text{THz,peak}}$ is the EO sampling signal at the peak position and α is the rotation angle of the QWP. $\alpha = 45°, 225°$ correspond to left circular polarization and $\alpha = 135°, 315°$ correspond to right circular polarization respectively, while $\alpha = 0°, 90°, 180°, 270°, 360°$ correspond to linear polarization. The last three terms in Eq. (1) have the same sign between $\alpha = 45°(225°)$ and $\alpha = 135°(315°)$, but the first term has opposite signs between the two QWP angles. Thus, parameter C expresses the helicity dependent contribution to the terahertz emission. Parameters L_1 and L_2 account for the linear photogalvanic effect or the photon drag effect, while parameter D represents a polarization-independent contribution, which includes thermal effects as well as drift currents and the photo-Dember effect [6,9,19]. The absolute values of the four fitting parameters are shown in Fig. 2(b). Of the four contributions,
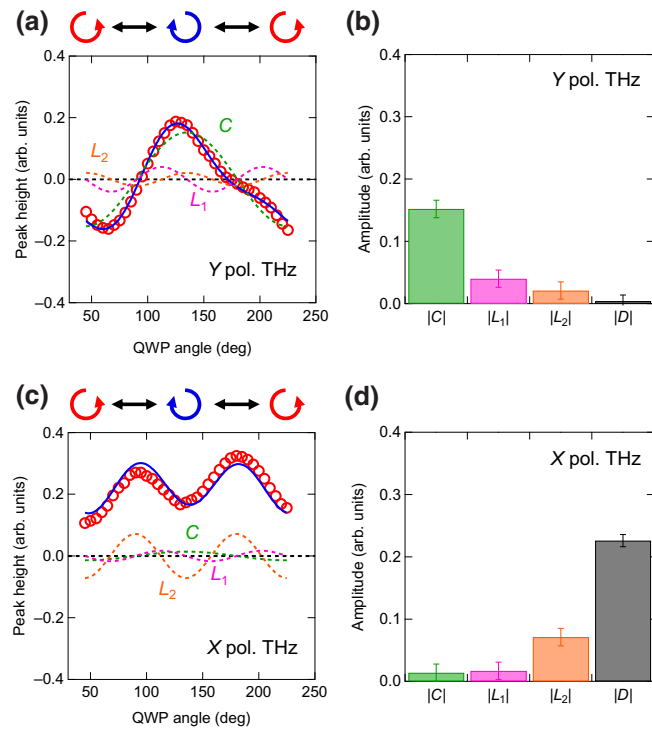
the helicity dependent contribution C is dominant in the Y polarized terahertz emission. The same analysis can be done for the X polarized terahertz emission as represented in Figs. 2(c) and 2(d). In contrast to Y polarized terahertz emission, the X polarized terahertz emission is dominated by the polarization-independent term.

To further understand the symmetry properties of this helicity dependent terahertz emission, we make additional measurements concerning the X polarized terahertz emission and the incident angle. Here we focus on the helicity dependent component of the terahertz emission, given by $S_{\text{THz,circ}}(t) = [S_{\text{THz},\sigma_-}(t) - S_{\text{THz},\sigma_+}(t)]/2$, where $S_{\text{THz},\sigma_-}(t)$ and $S_{\text{THz},\sigma_+}(t)$ are the waveforms of the EO sampling signal in the time domain when excited by left or right circularly polarized light, respectively. All waveforms displayed in Fig. 3 are those of $S_{\text{THz,circ}}(t)$ under different detection or excitation schemes.
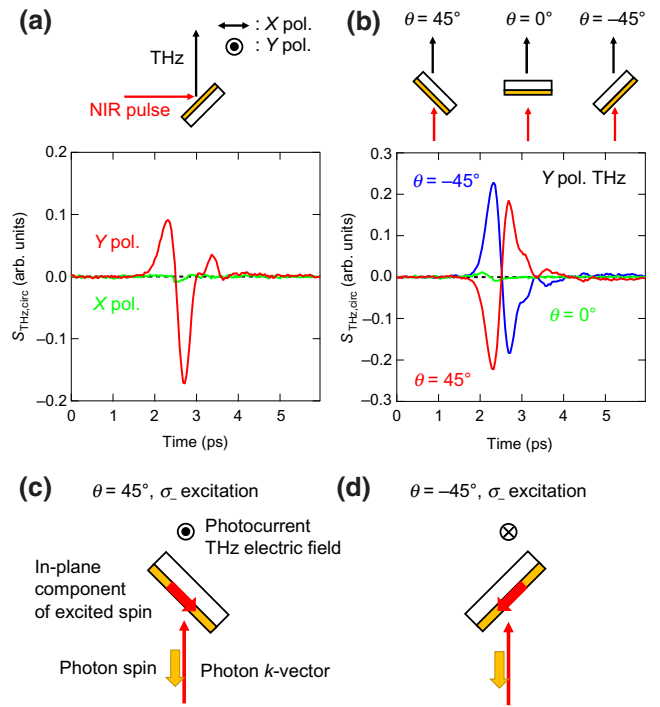

FIG. 2. (a) The peak EO sampling signal $S_{\text{THz,peak}}$ of the Y polarized terahertz wave from 30-nm-thick sample plotted against the rotation angle α of the QWP. The red circles are the experimental data and the blue solid line is the fitted result using Eq. (1). The dashed lines are the fitting results decomposed into each term of Eq. (1) except for the constant D. The green, magenta and orange dashed lines correspond to the contribution of the first, second, and third term in Eq. (1). (b) The absolute values of the fitting parameters obtained by the fitting shown in (a). (c), (d) Identical plots to (a) and (b) respectively, for X polarized terahertz waves.

FIG. 3. (a) Helicity dependent component of the X polarized terahertz wave (green) and the Y polarized terahertz wave (red) emitted from 30-nm-thick sample. See main text for the definition of $S_{\text{THz,circ}}$. A schematic of the measurement configuration is shown above. (b) Incident angle dependence of the helicity dependent component of the Y polarized terahertz wave emitted from 30 nm thick sample. The green waveform is obtained for normal incidence ($\theta = 0°$), while the red and blue waveforms are obtained for oblique incidence. Schematics of the measurement configuration are shown above. (c), (d) Schematic explaining the origin of the incident angle dependence (b) under the proposed photoinduced ISHE picture. Reversing the incident angle while holding the excitation helicity effectively reverses the in-plane component of the excited spin, causing the photoinduced spin current and the CPC to be odd with respect to the incident angle.

Figure 3(a) shows the comparison between $S_{\text{THz,circ}}(t)$ of the X polarized and the Y polarized terahertz wave. One can see that $S_{\text{THz,circ}}(t)$ is only apparent in the Y polarization; this is consistent with the results shown in Fig. 2. Figure 3(b) shows the incident angle dependence of $S_{\text{THz,circ}}(t)$ polarized in the Y direction. One can see that $S_{\text{THz,circ}}(t)$ is odd with respect to the incident angle and vanishes at normal incidence. Both of these features are typical for CPCs, and confirm that the helicity dependent terahertz emission is likely to be caused by ultrafast CPCs.

It is worth noting that the symmetric characteristics shown in Fig. 3 are expected for photocurrents from CPGE [9,10], CPDE [2,11], and photoinduced ISHE [15]. In order to determine the mechanism of the observed CPC, we study the thickness dependence of the terahertz emission. The results are shown in Fig. 4(a). Here we plot the results of the fitting using Eq. (1) at the peak position for each thickness. As one can see, the helicity dependent terahertz emission is enhanced by increasing the Bi layer thickness, until it saturates at around 70 nm. This indicates that there is a significant contribution that comes from the bulk of Bi. This excludes CPGE as a mechanism of CPCs,

since CPGE is only allowed at the surface of Bi, where inversion symmetry is broken. Moreover, the significant enhancement up to 70 nm cannot be explained by CPDE. This is because the penetration depth of NIR in Bi is about 15 nm [22]. Though CPDE is permitted in the bulk of Bi, it can only contribute within the penetration depth region, thus being incapable of explaining the enhancement up to 70 nm. The L_1 component also shows enhancement beyond the penetration depth of NIR in Bi. The origin of this enhancement remains unresolved, as contributions from the linear photogalvanic effect and photon drag effect should also show no significant enhancement in regions thicker than the penetration depth. However, we consider nonlocal effects, such as the diffusion of carriers, as a possible origin for the observed thickness dependence of the L_1 component. In fact, in the following we discuss how the enhancement of C can be explained by taking such effects into account.

IV. DISCUSSION

As the most plausible origin of the helicity dependent terahertz emission, we consider here the photoinduced ISHE. As schematically represented in Fig. 4(b), circularly polarized light with a tilted incidence angle can produce a gradient of in-plane spin polarization at the penetration depth region from the sample surface. The origin of the photoinduced spin polarization is likely to be attributed to the inverse Faraday effect [23–25], while the elucidation of the mechanism calls for further microscopic calculation based on the band structure of Bi, taking into account the spin-orbit interaction. The diffusion caused by such gradients then induces a spin current in the depth direction, which will be converted into a charge current, via the ISHE, that emits the terahertz waves. This picture is further supported by recent transport measurements suggesting that the photoinduced ISHE is the origin of CPCs in Bi thin films and Bi-based heterostructures where a similar thickness dependence was observed [26]. The incident angle dependence shown in Fig. 3(b) can also be understood by this picture. By reversing the incident angle while retaining the helicity, one is effectively reversing the in-plane component of the excited spin polarization, as shown in Figs. 3(c) and 3(d). Therefore, the sign of the spin current and the CPC becomes odd with respect to the incident angle, resulting in the symmetric feature observed in Fig. 3(b).

It should be noted here that the setup and mechanism of spin current generation in the present work is essentially different from that of Ref. [14], as the spin current is directly induced by the circularly polarized light excitation without any ferromagnetic layers or external magnetic fields. The pump-helicity dependent terahertz emission is also distinct from those observed in a ferromagnetic/nonferromagnetic metal heterostructure arising from the inverse spin-orbit torque [27] or ferromagnetic
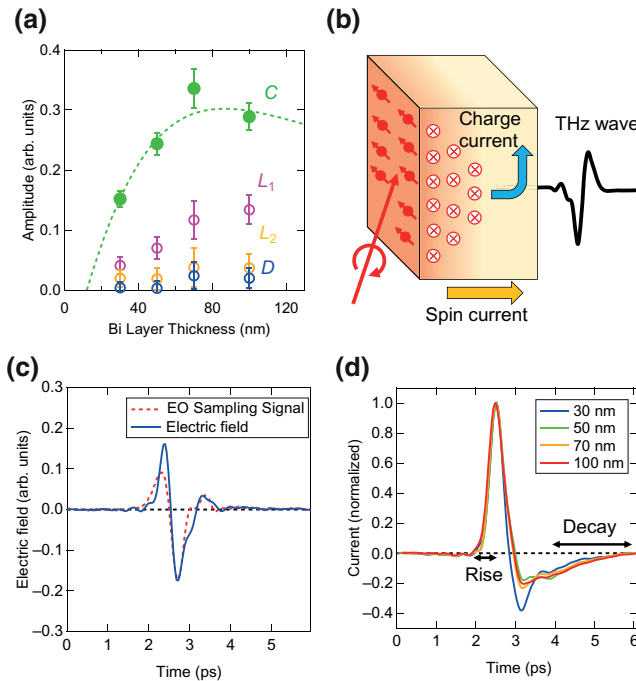

FIG. 4. (a) Bi layer thickness dependence of the terahertz emission. The green, magenta, orange and blue data points correspond to the absolute values of the fitting results C, L_1, L_2, and D using Eq. (1) at the peak position. The green dashed line is the fitting result using Eq. (2) with $\lambda_{\text{rel}} = 30$ nm. (b) Schematic of terahertz emission from photoinduced ISHE. (c) Extracted terahertz electric field (blue solid line) from 30-nm-thick sample along with the original EO sampling signal (red dashed line) plotted in the same scale for comparison. (d) Temporal dynamics of CPCs. Traces are normalized by their maximum value.

metal/Ag/Bi heterostructures where the inverse Rashba-Edelstein effect, the spin-to-charge conversion due to the Rashba surface state between Ag and Bi, is essential [28,29].

To analyze the thickness dependence of terahertz emitters using ISHE, we adopt the model used in Ref. [14], according to which the amplitude of terahertz emission as a function of thickness can be expressed as

$$E_{\text{THz}} \propto j_s^0 \frac{\lambda_{\text{rel}} \tanh[(d - d_D)/2\lambda_{\text{rel}}]}{1 + n_{\text{subst.}} + Z_0 \sigma d}, \qquad (2)$$

where d is the layer thickness, j_s^0 is the induced spin current in Bi, λ_{rel} is the characteristic relaxation length of the excited spins, $n_{\text{subst.}}$ is the refractive index of the substrate in the terahertz region, Z_0 is the impedance of free space, and σ is the optical conductivity of Bi in the terahertz region. We introduce the parameter d_D that accounts for the inactive dead layer of Bi. According to transport measurements, the thickness of this dead layer is estimated as $d_D \sim 12$ nm [26]. The parameter d_D is defined by the maximum Bi layer thickness at which helicity dependent photocurrents vanish. Note that optical properties, such as the refractive index of Bi, are not significantly influenced when the layer thickness is larger or smaller than d_D. The optical constants (refractive index and extinction coefficient) obtained from reflection and transmission measurements of the films, with Bi layer thickness below and above d_D, also agree well with those reported for bulk Bi [26,30]. $n_{\text{subst.}}$ and σ are measured using terahertz transmission spectroscopy and are determined as $n_{\text{subst.}} \sim 3.7$ and $\sigma \sim 1.4 \times 10^3$ S/cm. These quantities are almost constant across the range of 0.5–2.5 THz, and thus treated as constant values. The amount of spin polarization is assumed to be proportional to the absorbed number of photons. Since the penetration depth of NIR in Bi is about 15 nm, there should be no significant difference in the light absorption between the measured samples (with the thickness being over 30 nm), and thus j_s^0 is considered thickness independent.

Combining these considerations, Eq. (2) has only two free parameters, which are λ_{rel} and a global scaling parameter. We fit the thickness dependence in Fig. 4(a) with Eq. (2), as represented by the green dashed lines. From the fitting we obtain $\lambda_{\text{rel}} = 30 \pm 5$ nm, which is consistent with the relaxation length obtained from dc transport measurements, $\lambda_{\text{rel}} = 20 \pm 5$ nm [26]. Though photoinduced ISHE is usually neglected as a mechanism of CPCs because of the short spin relaxation time [9], the relatively long λ_{rel} suggests that such effects are capable of generating CPCs. This long relaxation length may originate from the high mobility or long lifetime of excited spins (due to low carrier density) in Bi [31]. The validity of this model may be further confirmed by time-resolved Kerr rotation

spectroscopy, which will give a measure of the spin's lifetime.

Finally, we briefly discuss the dynamics of CPCs. This information can be obtained by first calculating the terahertz electric field $E_{\text{THz,circ}}(t)$ from the EO sampling signal $S_{\text{THz,circ}}(t)$ and then integrating the terahertz electric field in the time domain. The first step requires a function that expresses the detection efficiency of the EO sampling setup [32–34]. Parameters are taken from Ref. [33]. The comparison of $S_{\text{THz,circ}}(t)$ and $E_{\text{THz,circ}}(t)$ is shown in Fig. 4(c), and the extracted CPCs are shown in Fig. 4(d) for different thicknesses. Here, the spectral component of the measured terahertz electric field above 3 THz is assumed to be zero, taking into account the detection bandwidth limit of the present EO sampling method. Figure 4(d) shows that the ultrafast CPC has a rise time of ∼0.3 ps and a decay time of ∼0.8 ps. The rise time of the transient current is almost comparable with the detection bandwidth of the present EO sampling method of the terahertz waveform. It is also worth noting that the observed decay time nearly coincides with values reported in pump-probe experiments of Bi [35–37], and may be related to the intervalley carrier scattering process.

We also notice from Fig. 4(d) that the current changes sign after the rapid decrease, which indicates the existence of backflowing currents. Since this feature is almost thickness independent, the backflow is unlikely to be explained by the reflection of spin currents at the Bi surface. This backflow may be explained by taking into account the photo-Dember effect. Here, the excited electrons and holes are spatially separated due to the difference in mobility, and thus form a dipole. If the electron-hole recombination is a slow process, the charge carriers can be accelerated by the dipole formed by themselves, resulting in a backflowing current. This scenario is supported by the two orders of magnitude difference in effective mass of photoexcited electrons and holes, and the long electron-hole recombination time of 4 ps [35]. Further investigation with high temporal resolution, e.g., with shorter laser pulses and broadband terahertz detection setups, combined with theoretical calculation taking into account the band structure of Bi would be promising for understanding the further detailed dynamics.

In conclusion, we demonstrate the circularly polarized light-induced terahertz emission from Bi thin films. The pump-helicity dependent component is most dominant in the terahertz wave polarized in the direction perpendicular to the plane of incidence, and obeys typical symmetry conditions which CPCs obey. Increasing the Bi layer thickness enhances the helicity dependent terahertz emission until it reaches saturation at around 70 nm. This thickness dependence is well explained by the photoinduced ISHE, indicating the unique character of Bi with relatively long spin diffusion length and large spin Hall angle. These results reveal the promising characters of Bi as a

platform for terahertz spintronics and other applications of terahertz technology, as well as the ability of terahertz emission spectroscopy as a probe for ultrafast spin and charge current dynamics.

ACKNOWLEDGMENTS

APPENDIX: INCIDENT ANGLE DEPENDENCE OF X POLARIZED TERAHERTZ WAVES

In Fig. 3(b), we show how the pump-helicity dependent terahertz emission polarized in the Y direction depends on the incident angle. While the pump-helicity dependent component is almost absent in the X polarized direction, we show here for a reference the X polarized terahertz emission in Fig. 5. The EO sampling signals in this direction vanish at normal incidence, and is odd with respect to the incident angle. In oblique incidence, the terahertz emission is enhanced when it is excited with linearly polarized light, which is consistent with Fig. 2(c). We note that the experimental setup for these data is different from those in the main text so that the terahertz waveforms appear different.
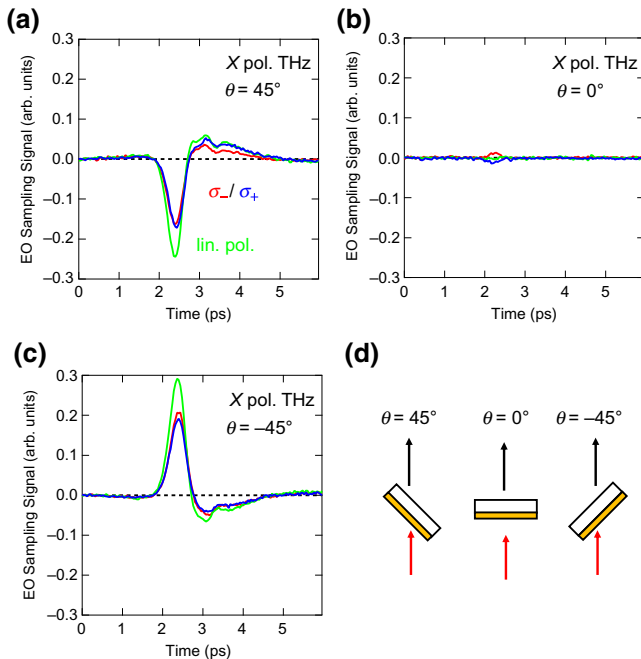

FIG. 5. (a), (b), (c) Waveforms of X polarized terahertz waves when the 30-nm-thick sample is excited by right circular polarization (σ_+), left circular polarization (σ_-), and linear polarization (lin. pol.), for different incident angles as schematically illustrated in (d).

[1] P. A. Obraztsov, N. Kanda, K. Konishi, M. Kuwata-Gonokami, S. V. Garnov, A. N. Obraztsov, and Y. P. Svirko, Photon-drag-induced terahertz emission from graphene, Phys. Rev. B **90**, 241416 (2014).

[2] L. Zhu, Z. Yao, Y. Huang, C. He, B. Quan, J. Li, C. Gu, X. Xu, and Z. Ren, Circular-Photon-Drag-Effect-Induced Elliptically Polarized Terahertz Emission From Vertically Grown Graphene, Phys. Rev. Appl. **12**, 044063 (2019).

[3] L. Braun, G. Mussler, A. Hruban, M. Konczykowski, T. Schumann, M. Wolf, M. Münzenberg, L. Perfetti, and T. Kampfrath, Ultrafast photocurrents at the surface of the three-dimensional topological insulator Bi_2Se_3, Nat. Commun. **7**, 13259 (2016).

[4] H. Takeno, S. Saito, and K. Mizoguchi, Optical control of spin-polarized photocurrent in topological insulator thin films, Sci. Rep. **8**, 8 (2018).

[5] N. Sirica, R. I. Tobey, L. X. Zhao, G. F. Chen, B. Xu, R. Yang, B. Shen, D. A. Yarotski, P. Bowlan, S. A. Trugman, J. X. Zhu, Y. M. Dai, A. K. Azad, N. Ni, X. G. Qiu, A. J. Taylor, and R. P. Prasankumar, Tracking Ultrafast Photocurrents in the Weyl Semimetal TaAs Using THz Emission Spectroscopy, Phys. Rev. Lett. **122**, 197401 (2019).

[6] Y. Gao, S. Kaushik, E. J. Philip, Z. Li, Y. Qin, Y. P. Liu, W. L. Zhang, Y. L. Su, X. Chen, H. Weng, D. E. Kharzeev, M. K. Liu, and J. Qi, Chiral terahertz wave emission from the weyl semimetal TaAs, Nat. Commun. **11**, 720 (2020).

[7] M. Chen, K. Lee, J. Li, L. Cheng, Q. Wang, K. Cai, E. E. M. Chia, H. Chang, and H. Yang, Anisotropic picosecond spin-photocurrent from weyl semimetal WTe_2, ACS Nano **14**, 3539 (2020).

[8] Y. Kinoshita, N. Kida, T. Miyamoto, M. Kanou, T. Sasagawa, and H. Okamoto, Terahertz radiation by sub-picosecond spin-polarized photocurrent originating from Dirac electrons in a Rashba-type polar semiconductor, Phys. Rev. B **97**, 161104 (2018).

[9] J. W. McIver, D. Hsieh, H. Steinberg, P. Jarillo-Herrero, and N. Gedik, Control over topological insulator photocurrents with light polarization, Nat. Nanotechnol. **7**, 96 (2012).

[10] P. Olbrich, L. E. Golub, T. Herrmann, S. N. Danilov, H. Plank, V. V. Bel'kov, G. Mussler, C. Weyrich, C. M. Schneider, J. Kampmeier, D. Grützmacher, L. Plucinski, M. Eschbach, and S. D. Ganichev, Room-Temperature High-Frequency Transport of Dirac Fermions in Epitaxially Grown Sb_2Te_3- and Bi_2Te_3-Based Topological Insulators, Phys. Rev. Lett. **113**, 096601 (2014).

[11] G. M. Mikheev, A. S. Saushin, V. V. Vanyukov, K. G. Mikheev, and Y. P. Svirko, Femtosecond circular photon drag effect in the Ag/Pd nanocomposite, Nanoscale Res. Lett. **12**, 39 (2017).

[12] Q. Ma, S. Y. Xu, C. K. Chan, C. L. Zhang, G. Chang, Y. Lin, W. Xie, T. Palacios, H. Lin, S. Jia, P. A. Lee, P. Jarillo-Herrero, and N. Gedik, Direct optical detection of Weyl fermion chirality in a topological semimetal, Nat. Phys. **13**, 842 (2017).

[13] J. Quereda, T. S. Ghiasi, J. S. You, J. van den Brink, B. J. van Wees, and C. H. van der Wal, Symmetry regimes for circular photocurrents in monolayer $MoSe_2$, Nat. Commun. **9**, 1 (2018).

[14] T. Seifert, *et al.*, Efficient metallic spintronic emitters of ultrabroadband terahertz radiation, Nat. Photonics **10,** 483 (2016).

[15] K. Ando, M. Morikawa, T. Trypiniotis, Y. Fujikawa, C. H. W. Barnes, and E. Saitoh, Photoinduced inverse spin-Hall effect: Conversion of light-polarization information into electric voltage, Appl. Phys. Lett. **96,** 1 (2010).

[16] D. Hou, Z. Qiu, K. Harii, Y. Kajiwara, K. Uchida, Y. Fujikawa, H. Nakayama, T. Yoshino, T. An, K. Ando, X. Jin, and E. Saitoh, Interface induced inverse spin Hall effect in bismuth/permalloy bilayer, Appl. Phys. Lett. **101,** 042403 (2012).

[17] C. Şahin and M. E. Flatté, Tunable Giant Spin Hall Conductivities in a Strong Spin-Orbit Semimetal: $Bi_{1-x}Sb_x$, Phys. Rev. Lett. **114,** 107201 (2015).

[18] Y. Fuseya, M. Ogata, and H. Fukuyama, Transport properties and diamagnetism of dirac electrons in bismuth, J. Phys. Soc. Japan **84,** 012001 (2015).

[19] H. Hirose, N. Ito, M. Kawaguchi, Y.-C. Lau, and M. Hayashi, Circular photogalvanic effect in Cu/Bi bilayers, Appl. Phys. Lett. **113,** 222404 (2018).

[20] S. A. Stanley and M. D. Cropper, Structure and resistivity of bismuth thin films deposited by pulsed DC sputtering, Appl. Phys. A Mater. Sci. Process. **120,** 1461 (2015).

[21] D. L. Partin, J. Heremans, D. T. Morelli, C. M. Thrush, C. H. Olk, and T. A. Perry, Growth and characterization of epitaxial bismuth films, Phys. Rev. B **38,** 3818 (1988).

[22] E. G. Gamaly and A. V. Rode, Ultrafast electronic relaxation in superheated bismuth, New J. Phys. **15,** 013035 (2013).

[23] A. Kirilyuk, A. V. Kimel, and T. Rasing, Ultrafast optical manipulation of magnetic order, Rev. Mod. Phys. **82,** 2731 (2010).

[24] I. D. Tokman, Q. Chen, I. A. Shereshevsky, V. I. Pozdnyakova, I. Oladyshkin, M. Tokman, and A. Belyanin, Inverse Faraday effect in graphene and Weyl semimetals, Phys. Rev. B **101,** 174429 (2020).

[25] M. Kawaguchi, H. Hirose, Z. Chi, Y.-C. Lau, F. Freimuth, and M. Hayashi, Giant inverse Faraday effect in Dirac semimetals, arXiv:2009.01388.

[26] H. Hirose, M. Kawaguchi, Y.-C. Lau, F. Freimuth, and M. Hayashi, arXiv:2011.06786.

[27] T. J. Huisman, R. V. Mikhaylovskiy, J. D. Costa, F. Freimuth, E. Paz, J. Ventura, P. P. Freitas, S. Blügel, Y. Mokrousov, T. Rasing, and A. V. Kimel, Femtosecond control of electric currents in metallic ferromagnetic heterostructures, Nat. Nanotechnol. **11,** 455 (2016).

[28] M. B. Jungfleisch, Q. Zhang, W. Zhang, J. E. Pearson, R. D. Schaller, H. Wen, and A. Hoffmann, Control of Terahertz Emission by Ultrafast Spin-Charge Current Conversion at Rashba Interfaces, Phys. Rev. Lett. **120,** 207207 (2018).

[29] C. Zhou, Y. P. Liu, Z. Wang, S. J. Ma, M. W. Jia, R. Q. Wu, L. Zhou, W. Zhang, M. K. Liu, Y. Z. Wu, and J. Qi, Broadband Terahertz Generation via the Interface Inverse Rashba-Edelstein Effect, Phys. Rev. Lett. **121,** 086801 (2018).

[30] W. S. M. Werner, K. Glantschnig, and C. Ambrosch-Draxl, Optical constants and inelastic electron-scattering data for 17 elemental metals, J. Phys. Chem. Ref. Data **38,** 1013 (2009).

[31] H. Emoto, Y. Ando, G. Eguchi, R. Ohshima, E. Shikoh, Y. Fuseya, T. Shinjo, and M. Shiraishi, Transport and spin conversion of multicarriers in semimetal bismuth, Phys. Rev. B **93,** 174428 (2016).

[32] T. Kampfrath, J. Nötzold, and M. Wolf, Sampling of broadband terahertz pulses with thick electro-optic crystals, Appl. Phys. Lett. **90,** 231113 (2007).

[33] S. Casalbuoni, H. Schlarb, B. Schmidt, P. Schmüser, B. Steffen, and A. Winter, Numerical studies on the electro-optic detection of femtosecond electron bunches, Phys. Rev. Spec. Top. Accel. Beams **11,** 072802 (2008).

[34] B. Wu, L. Cao, Z. Zhang, Q. Fu, and Y. Xiong, Terahertz electro-optic sampling in thick ZnTe crystals below the reststrahlen band With a broadband femtosecond laser, IEEE Trans. Terahertz Sci. Technol. **8,** 305 (2018).

[35] I. Timrov, T. Kampfrath, J. Faure, N. Vast, C. R. Ast, C. Frischkorn, M. Wolf, P. Gava, and L. Perfetti, Thermalization of photoexcited carriers in bismuth investigated by time-resolved terahertz spectroscopy and *ab initio* calculations, Phys. Rev. B **85,** 155139 (2012).

[36] J. Faure, J. Mauchain, E. Papalazarou, M. Marsi, D. Boschetto, I. Timrov, N. Vast, Y. Ohtsubo, B. Arnaud, and L. Perfetti, Direct observation of electron thermalization and electron-phonon coupling in photoexcited bismuth, Phys. Rev. B **88,** 075120 (2013).

[37] Y.-H. Cheng, F. Y. Gao, S. W. Teitelbaum, and K. A. Nelson, Coherent control of optical phonons in bismuth, Phys. Rev. B **96,** 134302 (2017).